ADVANCED OPTICAL MATERIALS

www.advopticalmat.de

Check for updates

Integration of MoS_2 with InAlAs/InGaAs Heterojunction for Dual Color Detection in Both Visible and Near-Infrared Bands

Jianan Deng, Lingyi Zong, Wenzhong Bao, Mingsai Zhu, Fuyou Liao, Zhongxun Guo, Yuying Xie, Bingrui Lu, Jing Wan, Jiahe Zhu, Ruwen Peng, and Yifang Chen**

At present, dual-channel or even multi-channel recording is a developing trend in the field of photodetection, which is widely applied in environment protection, security, and space science and technology. This paper proposes a novel MoS_2/InAlAs/InGaAs n–i–n heterojunction phototransistor by integrating multi-layered MoS_2 with InGaAs-based high electron mobility transistors (InGaAs-HEMTs). Due to the internal photocurrent amplification in the InGaAs channels with a narrow energy bandgap of 0.79 eV, this device exhibits high photoresponsivity (R) of over 8×10^5 A W^{-1} under near-infrared illumination of 1550 nm at 500 pW. Furthermore, with the combination of the photoconductance effect in the vertical MoS_2/InAlAs/InGaAs n–i–n heterojunction and the photogating effect in the lateral phototransistor, this device possesses a unique characteristic under visible illumination that its photoresponsivity can be tuned by the top gate electrode from 6×10^5 A W^{-1} to -4×10^5 A W^{-1} by gate voltage. This may lead to a new application as an optically controlled electronic inverter, which needs further study in depth. This MoS_2/InAlAs/InGaAs phototransistor builds up a new bridge between 2D materials and conventional ternary compounded semiconductor devices.

The trend of photoelectric detection is advancing toward multiband detection, miniaturization, and high integration within one substrate. To accomplish multichannel detection to broadband electromagnetic radiation, independent photodetectors based on different semiconductors—such as GaN[1,2] for ultraviolet (UV), Si[3,4] for visible, and InGaAs[5,6] for near-infrared (NIR) bands—are usually assembled in one imaging system. However, such a conventional technique is being challenged by the demand for system miniaturization. So far, several methods have been proposed to extend the response spectra of a single photodetector. One method involves heterogeneously integrating photodetectors based on materials with different bandgaps (such as Si and III–V compounds) on the same substrate by molecular beam epitaxy (MBE) or metal organic chemical vapor deposition (MOCVD) to introduce extra absorption layers.[7–10] Unfortunately, owing to lattice mismatches, significant leakage current frequently occurs in the dark, and the manufacturing is complicated and expensive. Another approach is to integrate a metasurface into a semiconductor by local plasmonic resonances.[11–15] However, such detectors suffer from extremely low quantum efficiency due to energy loss in the metallic metasurface.

In recent years, 2D materials based on van der Waals heterojunctions have been extensively investigated as potential candidates for next-generation optoelectronic devices.[16–18] Different from conventional bulk semiconductors with covalent bonds, the lack of dangling bonds at the surface of 2D materials enables the realization of interfaces with fewer defects and lattice mismatches than conventional semiconductor devices,[19] offering us an excellent opportunity to integrate 2D materials with conventional

J. Deng, M. Zhu, Y. Xie, Prof. B. Lu, Prof. J. Wan, Prof. Y. Chen
State Key Laboratory of ASIC and System
School of Information Science and Technology
Fudan University
Shanghai 200433, China
E-mail: yifangchen@fudan.edu.cn

L. Zong, Prof. W. Bao, F. Liao, Z. Guo
State Key Laboratory of ASIC and System
School of Microelectronics
Fudan University
Shanghai 200433, China
E-mail: baowz@fudan.edu.cn

Prof. J. Zhu
School of Electronic Science and Engineering
Nanjing University
Nanjing 210093, China

Prof. R. Peng
National Laboratory of Solid State Microstructures
School of Physics
and Collaborative Innovation Center of Advanced Microstructures
Nanjing University
Nanjing 210093, China

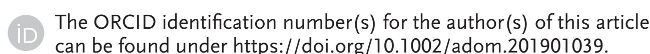
The ORCID identification number(s) for the author(s) of this article can be found under https://doi.org/10.1002/adom.201901039.

DOI: 10.1002/adom.201901039

© 2019 WILEY-VCH Verlag GmbH & Co. KGaA, Weinheim

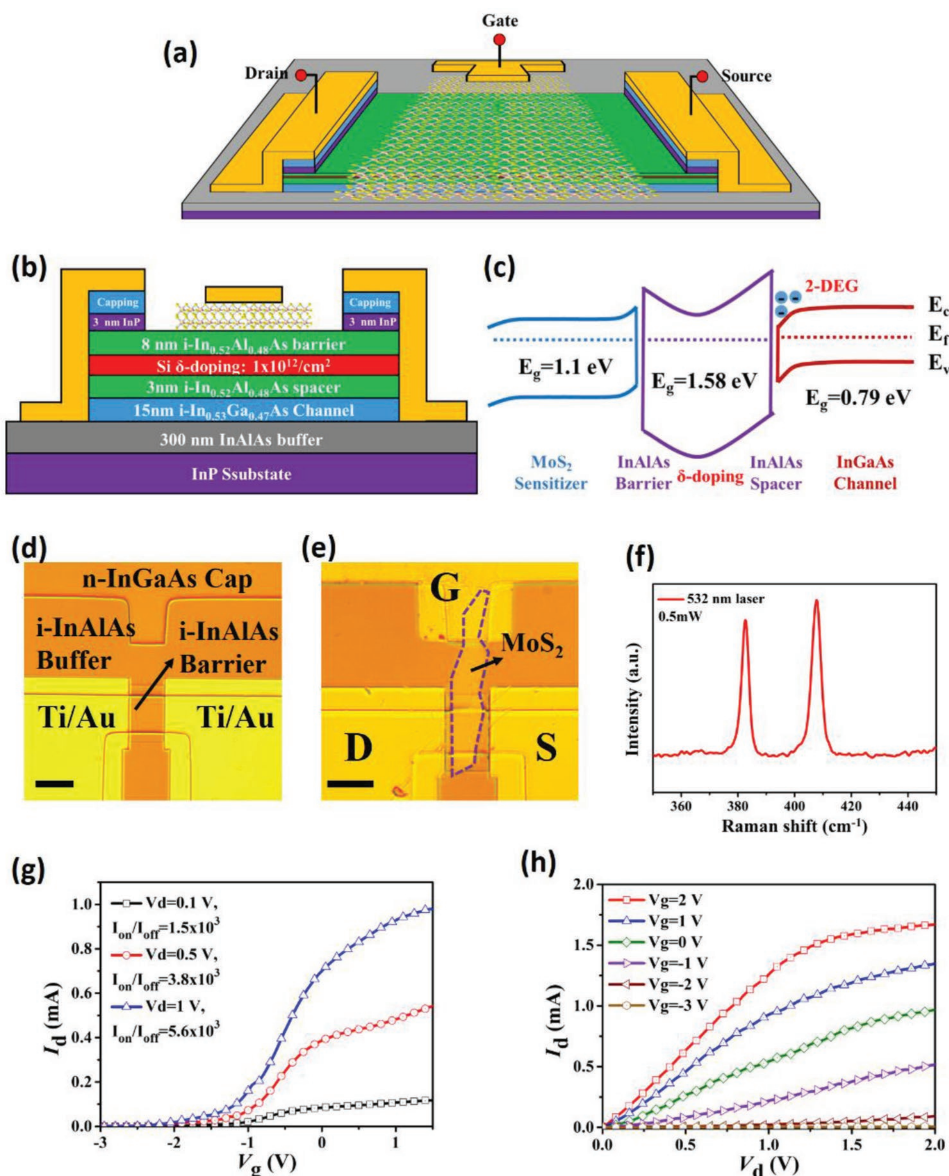

Figure 1. The measured basic property of the fabricated device. a,b) Layer structure as well as the device structure in a MoS_2/InAlAs/InGaAs phototransistor. c) Energy band diagram of the MoS_2/InAlAs/InGaAs heterojunction. d,e) Optical image of the fabricated HEMT and the MoS_2 gate covered one, both the scale bars are 10 µm. f) Measured Raman spectrum of the MoS_2 flake. g) The transfer characteristic with different drain voltages. h) Output characteristic of the HEMT with different gate voltages through the MoS_2 flake.

semiconductors for novel optoelectronic devices. In this work, a new phototransistor based on 2D/3D MoS_2/InAlAs/InGaAs n-i-n heterojunction has been proposed to achieve photodetection in both visible and NIR bands. Different from conventional photogating transistors,[20–22] an electrode is connected to the top MoS_2 in order to control the carrier density in the 2D electron gas (2-DEG) at the InAlAs/InGaAs interface. When the device is exposed to visible light, photocarriers generated in the top MoS_2 may lead to the photoconductance effect as well as the photogating effect combined with the lateral phototransistor beneath it. Thus, the photoresponsivity, R, can be tuned between positive and negative values by adjusting the biases to the MoS_2 gate. A positive R of 6×10^5 A W^{-1} is obtained at $V_g = -2$ V under light illumination at the wavelength of 500 nm. With the increase of V_g under the same illumination condition, R gradually decreases to -4×10^5 A W^{-1} at $V_g = +1$ V. When the device is illuminated by NIR light, the photovoltaic effect induced by photoholes accumulated in the InGaAs channel may reduce the barrier between the source and the conducting channel, leading to a remarkable boost of the drive current from the source to the drain. Such a unique characteristic is beyond previously reported monopolar photoresponsivity,[23,24] suggesting that the proposed device is actually a dual-band photoelectron detector responsible in both visible and NIR wavelengths.

Figure 1a displays the structure of the MoS_2/InAlAs/InGaAs heterojunction phototransistor. The device is initially based on a

© 2019 WILEY-VCH Verlag GmbH & Co. KGaA, Weinheim

typical high electron mobility transistor (HEMT) with InGaAs/InAlAs heterojunction grown by MBE on a semi-insulating InP substrate,[25,26] as illustrated by the layer structure in Figure 1b. The doping level in the Si δ-doping layer is 1×10^{12} cm^{-2} (n-type), and the 20 nm $In_{0.53}Ga_{0.47}As$ capping layer is heavily doped with the density of approximately 1×10^{19} cm^{-3} (n-type). The energy band diagram of the device along the vertical direction shown in Figure 1c indicates that the 2-DEG may be accumulated at the InAlAs/InGaAs interface, which ensures high electron mobility in the InGaAs channel layer. Meanwhile, the Vanderbilt Hall testing and the transmission line method (TLM) are applied to measure the electron mobility of 8120 cm^2 V$^{-1}\cdot$s^{-1} and the contact resistance of 0.04 Ω·mm (see Figure S1 in the Supporting Information). The phototransistors are then fabricated by a standard HEMT process flow, including mesa isolation, S/D contact, and gate recess etching (the details of the fabrication process are summarized in the Experimental Section), as shown by the optical microscopic image in Figure 1d.[27] On the fabricated HEMT, a multilayer MoS_2 sheet is subsequently transferred onto the recessing-exposed InAlAs barrier layer. Finally, a 10 nm Ti/100 nm Au is deposited to connect the end of the MoS_2 so that the whole device becomes a MoS_2/InAlAs/InGaAs heterojunction phototransistor, as shown in Figure 1e. Both the width and the length of this phototransistor are 10 µm, which defines the effective photon sensitive area of the phototransistor as 100 µm^2. Raman spectroscopic characterization of the MoS_2 sheet is shown in Figure 1f. The peak position of E^1_{2g} is around 382 cm^{-1} and that of A_{1g} is around 407 cm^{-1}, which confirms that the transferred MoS_2 sheet has multiple layers, and the thickness is determined to be 12 nm by atomic force microscopy (AFM), as shown in Figure S2 in the Supporting Information.

Basic electrical characterizations of the MoS_2/InAlAs/InGaAs phototransistor are carried out in the dark. The measured I_d (drain current)-V_g (top gate voltage) characteristics of the fabricated device are presented in Figure 1g. The device functions as a depletion-mode n-type field effect transistor (FET), with the MoS_2 sheet acting as an effective gate to electrostatically control the current through the InGaAs channel. The source–drain current (I_d) increases to 1 mA as V_g increases from −3 to 1.5 V at a fixed V_d = +1 V, with a threshold voltage (V_{th}) of −1.5 V and a current on/off ratio of 5.6×10^3, which is comparable with that in a conventional InGaAs/InAlAs HEMT.[28] The leakage current between the isolations through the intrinsic buffer layer is also measured, as shown in Figure S3 in the Supporting Information. It is reduced to 2.5×10^{-9} A when V_d = +1 V, which is negligible compared with the channel current. The $I_d - V_d$ output characteristics display a saturation region when under large V_d and positively biased V_g (**Figure 2**h), which is also similar to a standard n-type FET.

Having established the basic electrical performance of the device, the optoelectronic property of the device is then systematically studied. Figure 2a presents the I_g–V_g electrical characteristics of the two embedded vertical

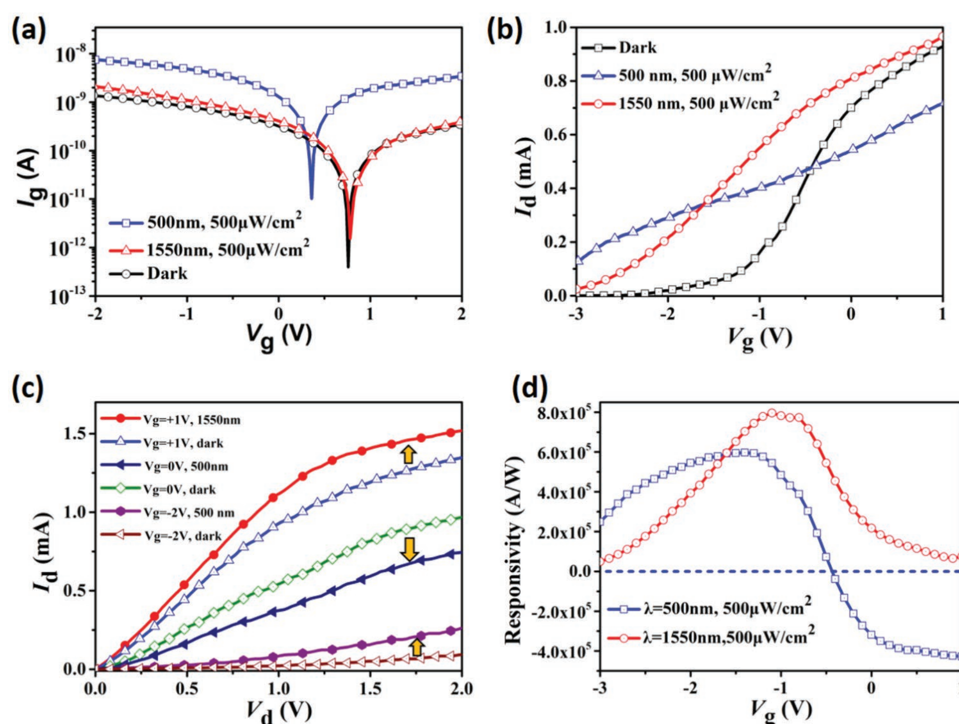

Figure 2. Photoresponse in the embedded MoS_2/InAlAs/InGaAs heterojunction. a) I_g–V_g curves of the embedded MoS_2/InAlAs/InGaAs heterojunction in the dark and under visible/NIR illumination, respectively. b) Device transfer curves under dark and visible/NIR illumination. The gate voltage below −0.5 V should be the working area for the dual color detector. c) Output curves under visible and NIR illumination with different gate voltage biases, indicating negative and positive photo response can be both achieved. d) Relation between V_g and R: a peak value of 6×10^5 A W^{-1} and a valley value of -4×10^5 A W^{-1} can be obtained. The peak positions of the responsivity for both the visible and the NIR illumination are close to the maximum transfer conductance, which explains the origin of the high responsivity.

© 2019 WILEY-VCH Verlag GmbH & Co. KGaA, Weinheim

MoS_2/InAlAs/InGaAs heterojunctions with the phototransistor, where one heterojunction is terminated with the gate-source electrodes and the other heterojunction is terminated with the gate–drain electrodes. Since the InAlAs barrier is electrically intrinsic and the InGaAs layer is partially n-doped by 2-DEG, the two heterojunctions behave like an n-i-n junction without the built-in electric field, giving rise to a symmetric I_g–V_g curve in the dark when V_g sweeps from −1 to +2 V, with the valley point occurring at V_g = +0.8 V. When the device is subjected to visible illumination, the I_g – V_g curve is still symmetric but undergoes an upper-left shift. When the device is subjected to NIR illumination, no observable shift is seen in the I_g–V_g curve, implying that no additional photocurrent is generated by the top gate electrode.

The origin of the shift can be clearly interpreted by the currents flowing through the equivalent circuit to the two-heterojunction system under different gate biases and illumination conditions, as schematically illustrated in Figure S4a–c in the Supporting Information. In the circuit, the MoS_2/InAlAs/InGaAs heterojunction can be represented by two resistors: R_g and R_c. R_g is the total serial resistance including the MoS_2 intrinsic resistance, the contact resistance between the MoS_2 and the metal gate, and the one between the MoS_2 and the InAlAs barrier. R_c represents the conductive resistance of the InGaAs channel, which is apparently much smaller than R_g.

In the dark condition with V_d = +1 V and V_s = 0 V, as shown in Figure S4a in the Supporting Information, the net current I_g is $I_1 + I_2$, where I_1 originates from one of the two MoS_2/InAlAs/InGaAs heterojunctions, and I_2 originates in the other heterojunction. When V_g = +0.8 V, I_1 and I_2 have the same magnitude but flow in the opposite directions, leading to the minimum net current I_g. However, such a balance is broken when visible light at 500 nm shines on the device, and the photocurrent generated in the MoS_2 shifts the minimum point to V_g = +0.3 V, at which time a new balance with $I_1 + I_2 + I_{MoS2} = 0$ is established, as described in Figure S4b in the Supporting Information. When the device is illuminated by NIR radiation at 1550 nm, photocarriers are generated only in the InGaAs channel because the MoS_2 is does not respond to illumination of NIR. Since $R_g > R_c$, where R_c is the sheet resistance of InGaAs, the photogenerated electrons are directly collected by the drain electrode as illustrated by the red arrow in Figure S4c in the Supporting Information, and the photogenerated holes are trapped in the quantum well in the InAlAs/InGaAs heterojunction. Therefore, the I_g – V_g curve is not affected by the NIR illumination, as shown by the red curve in Figure 2a.

The photogating effect by the MoS_2 layer on the transfer characteristics of the phototransistor is also studied. Figure 2b presents the transfer curves of the InP-HEMT gated by the MoS_2 layer. Three transfer curves are measured in the dark (the black curve), under visible illumination at 500 nm (the blue curve), and under NIR radiation at 1550 nm (the red curve). When V_g < −0.5 V, the dark current is lower than the current under visible illumination, when the phototransistor behaves like a normal phototransistor. When V_g = −0.5 V, the two curves intersect at one point, which indicates that there is no photogating effect under this bias. It is surprising to find that when V_g > −0.5 V, the dark current gradually becomes higher than the light current, and the device obtains a negative photoresponse. While under the illumination at 1550 nm, as the MoS_2 layer is transparent to NIR light, the photogenerated electrons and holes only appear in the InGaAs channel. The measured transfer curve (the red curve) in Figure 2b exhibits a leftward shift, which indicates a positive photoresponse in a traditional InGaAs-based HEMT.[29–33] Such a photoelectric characteristic has also been shown in the I_d–V_d output curves in **Figure 3**c. Under visible illumination of 500 nm, the device obtains positive photo response with V_g = −2 V. When V_g = 0 V, the device has a negative photo response. Under NIR illumination of 1550 nm, the device has a positive photo response with V_g = +1 V.

The photoelectronic responsivity (R) under different V_g in visible/NIR illumination is presented in Figure 2d, where R is defined as $I_{ph}/(P \times A)$, I_{ph} is the photocurrent, P is the intensity of the incident light, and A is the sensing area of the photodetector. Under the visible illumination, R rises from 2×10^5 A W^{-1} to the peak value of 6×10^5 A W^{-1} when V_g changes from −3 to −1.5 V. During the V_g sweeping, the increase of the device transconductance gives rise to a boost of R. Sweeping V_g from −1.5 to −0.5 V, R drops rapidly from the peak value to 0 A W^{-1}. Further sweeping the gate voltage beyond −0.5 V, R drops to a negative value and finally reaches the minima of -4×10^5 A W^{-1}. This ambipolar responsivity tuned by the bias makes this device a great prospect for the optically controlled electronic inverter.[34] Again, under the NIR illumination, R shows the conventional behavior because the MoS_2 layer is not involved in the optoelectronic process of the device. The peak point of 8×10^5 A W^{-1} at V_g = −0.5 V is measured.

To further demonstrate the abnormal negative photoresponse in the visible band and the extremely high photoresponsivity in the NIR band, the energy band diagrams along the vertical and lateral directions are shown in Figure 3. Under the visible illumination, the drain current (I_d) is reduced for V_g > −0.5 V. Because the energy band bends downward as shown in Figure 3a, the photogenerated electrons in the top MoS_2 flow to the gate metal electrode, generating an additional voltage drop on the MoS_2 flake and reducing the effective gate voltage V_g' as $V_g' = V_g - I_g \times R_g$, where I_g is the photocurrent in the MoS_2, and R_g is the parasitic resistance of the MoS_2 gate as mentioned before. The effective gate voltage V_g' leads to an amplification of the drain current through the InGaAs channel layer. Meanwhile, due to the low energy band off set between MoS_2 and InAlAs, the photogenerated holes may be collected by the source and drain electrodes. As illustrated by the lateral energy band diagram in the InGaAs layer shown in Figure 3d, the energy barrier beneath the MoS_2-overlapped region is higher than that in the dark condition (the green and dark lines); the increase of the barrier in the dark results in the reduction of the drain current I_d and thus a negative photoresponse.

For V_g < −0.5 V, as shown in Figure 3b,e, the photogenerated holes in the MoS_2 flow to the gate, leading to the increase of V_g' as $V_g' = V_g + I_g \times R_g$ and resulting in the lowering of the energy barrier beneath the MoS_2 overlapped region and the boost of the drain current, while the photogenerated electrons may be collected by the S/D electrodes. When V_g = −0.5 V, these two curves intersect with each other, corresponding to the situation without the photogating effect. Here, the band bending between

© 2019 WILEY-VCH Verlag GmbH & Co. KGaA, Weinheim

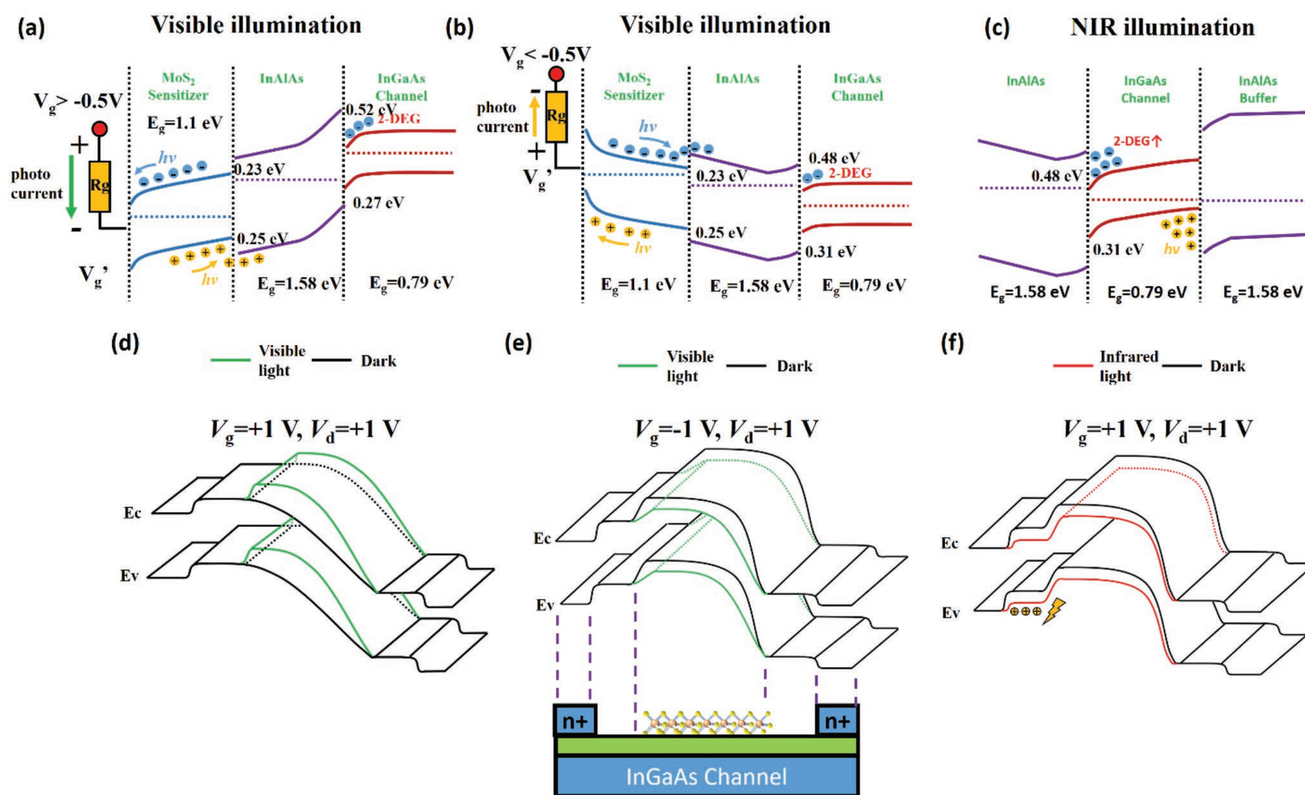

Figure 3. The energy band diagram of the MoS2/InAlAs/InGaAs phototransistor. a,b) Energy band diagram of MoS_2/InAlAs/InGaAs along the vertical side with different gate voltage biases in visible light. c) Energy band diagram of InAlAs/InGaAs/InAlAs along the vertical side in NIR light, indicating an effective separation of the photogenerated electrons and holes in the InGaAs channel. d–f) Lateral energy band diagram along the InGaAs channel under visible/NIR illumination to illustrate the amplification of the photocurrent in the phototransistor.

the gate metal and the MoS_2 layer is diminished, leading to no photocarriers flowing into the gate electrode. All in all, the existence of the MoS_2 as the gate on the InP-HEMT causes the clockwise rotation of the transfer curve of the InAlAs/InGaAs phototransistor under the condition of visible illumination.

Under the illumination at 1550 nm, as the MoS_2 layer is transparent to NIR light, the photogenerated electrons and holes only appear in the InGaAs channel. Taking $V_g = +1$ V and $V_d = +1$ V as an example, and the internal gain in the InGaAs channel can be explained by the energy band diagram illustrated in Figure 3c,f. Due to the vertically built-in electric field induced by the δ-doping layer, the photogenerated holes will hardly be recombined with the electrons in the the 2-DEG and will be accumulated at the bottom interface of InGaAs channel, as presented in Figure 3c.

Meanwhile, the lateral electric field beneath the MoS_2 gate is rather large, thus the photogenerated electrons in the InGaAs channel can be quickly collected by the drain electrode, while the photoholes drift toward the source. Due to the heavily n-doped capping layer as shown in Figure 1a, the energy band beneath the capping layer bends downward, leading to the accumulation of photogenerated holes near the source electrodes. These accumulated holes finally diminish the barrier of the conducting channel, leading to a boost of the drive current I_d.

The response speed of the device to 1 Hz modulated incident light in the form of a square waveform is measured under a fixed V_d = +1 V. **Figure 4**a,b present the measured photoelectronic currents in response to the visible light. With $V_g = +2$ V, the rise and fall times in the measured photocurrent

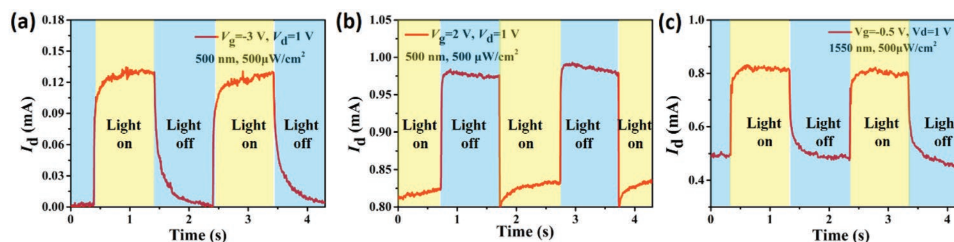

Figure 4. The transient characteristics of the device under different gate biases and illumination conditions. a,b) The positive/negative photoresponse speed under visible illumination. c) The photoresponse speed of the device under NIR illumination.

© 2019 WILEY-VCH Verlag GmbH & Co. KGaA, Weinheim

waves define the response times as 4 ms for the current rise and 6 ms for the fall. With $V_g = -3$ V, the response times are 11 ms for the rise and 200 ms for the fall in the photocurrent. Clearly, the negative response has a faster speed. Such a difference in the response time hints that the working speed of the phototransistor can be tuned according to the conduction state dominated by either the minority or majority carrier. Figure 4c shows the transient characteristics under NIR illumination at 1550 nm. The rise/fall time of the photocurrent is 14 and 70 ms, respectively. As the gate in our phototransistor is a semiconductor, the gate resistance is much larger than that in a conventional metal gate, which may induce a higher RC delay and a lower response speed. The resistance of MoS_2 can be extracted as over 10^8 Ω by the I_g–V_g curve in darkness and visible illumination in Figure 2a using the equation given by

$$R = \frac{\Delta V_g}{\Delta I_g} \tag{1}$$

Meanwhile, as the width of the device is 10 µm, the photogenerated electrons and holes in MoS_2 need a higher drifting time before they are collected by the gate metal electrode. Such a drifting time greatly influence the device response speed. Because the electrons have a higher drifting speed than holes, the negative response speed can be faster than the positive response speed.

The I_d–V_g curves under different illumination intensities of 100, 500, and 800 µW cm^{-2} are shown in **Figure 5**a. It is rather interesting to see that all three curves display a clockwise rotation around the intersection point at $V_g = -0.5$ V. The rotation angle is positively related to the intensity; it can be understood that a higher intensity gives rise to a larger voltage drop on the MoS_2. With the intensity increasing, I_d gradually approaches the green line with the highest light intensity, which is the same as the behavior of the device without the MoS_2 gate. It can then be concluded that with the light intensity increasing, the photogating effect of the MoS_2 on the InGaAs channel gradually weakens. In contrast, the I_d–V_g curves under different

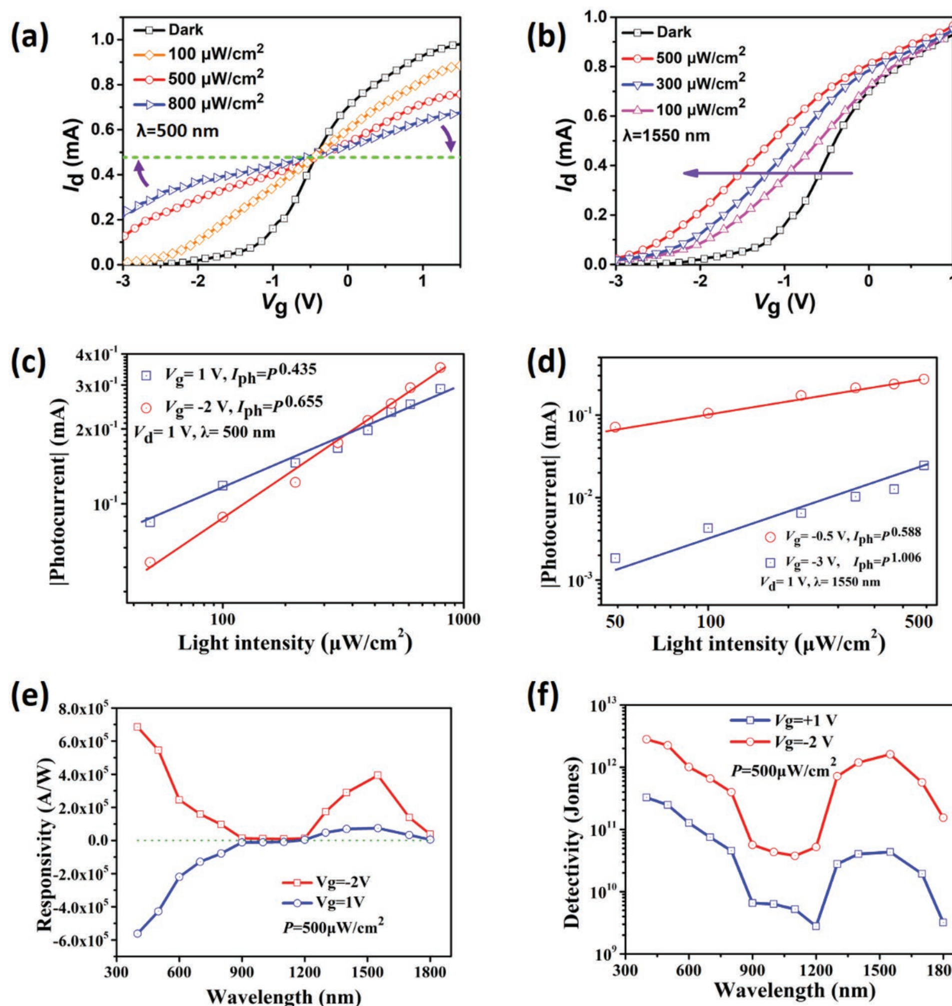

Figure 5. The comprehensive properties of MoS_2/InAlAs/InGaAs phototransistor. a,b) I_d–V_g curves under different light intensities in visible and NIR bands. c,d) Both the measured and fitted curves of the relation between photocurrent and light intensity under different V_g biases in visible and NIR illumination. e) The measured spectra of the photoresponsivity. f) The measured spectra of the detectivity. Both the responsivity and the detectivity show the detection peaks in both the visible and NIR regions.

© 2019 WILEY-VCH Verlag GmbH & Co. KGaA, Weinheim

NIR illumination intensities do not exhibit clockwise rotation. Instead, the drain currents are increased with the increasing intensity (Figure 5b) as normal.[33]

Figure 5c,d depicts the photocurrent in the phototransistor as a function of light intensity under different V_g and light bands. Similar to the previously reported detectors with photogating effect, the measured photocurrents follow the relationship as expressed by the following equation

$$|I_{ph}| = |\Delta V_{th} G_m| \propto P^{\alpha} \tag{2}$$

where I_{ph} is the difference between light current and dark current, P is the light intensity, α is the fitting parameter related to the gate voltage,[24] ΔV_{th} is the threshold voltage shift induced by the photo gate, and G_m is the device transconductance. Thus, the amplified photo current is much related to the gate voltage bias. The straight lines in Figure 5c,d are the fitting results when α values of 0.44 and 0.66 are used for V_g of +1 and −2 V, respectively. The photocurrent has a better linearity with the light power intensity when $V_g = -2$ V. Under the NIR illumination, α is fitted to be 0.588 and 1.006 at V_g of −0.5 and −3 V, respectively.

Figure 5e shows the responsivity spectra for the MoS_2/InAlAs/InGaAs heterojunction phototransistor. The spectra cover the visible bands from 400 to 800 nm as well as from 1100 to 1800 nm. The vertical MoS_2/InAlAs/InGaAs n-i-n heterojunction as the integration of the MoS_2 to the InP-HEMT clearly demonstrates its multifunctionality as a dual color detector in both visible light and the wavelength of 1550 nm. The responsivity spectra are very similar to those from the MoS_2- and InGaAs-based photodetectors.[6,35]

Apart from the responsivity, the detectivity D^* is also characterized, D^* can be expressed by the following equation

$$D^* = \frac{A^{1/2} * R}{(2q\, I_{dark})^{1/2}} \tag{3}$$

Figure 5f presents the D^* spectra under $V_g = -2$ and +1 V. Obviously D^* is much larger at $V_g = -2$ V than that at +1 V because of the lower dark current when the device is turned off. In the visible band, the photoelectron gating effect by the MoS_2 layer dominates the detection mechanism. The detectivity starts at the level of $D^* = 3 \times 10^{12}$ Jones at the wavelength of 400 nm and then decreases to 3×10^{10} Jones at 900 nm, which is in the near-infrared region. In the near-infrared region, the detectivity D* of the device reaches the peak of 2×10^{12} Jones at 1550 nm. Such D^* is comparable with that in conventional Si-, Ge-, and InGaAs-based photodetectors.[36] With the optoelectronic response in both visible and NIR regions, the proposed MoS_2/InAlAs/InGaAs phototransistor can function as an integrated detector for dual color detection in both visible and near-infrared regions. Such a novel detector should find extensive applications in imaging techniques such as space technology, earth observation, environment protection, security, and 24 h monitoring.

This work has successfully developed a novel dual color photoelectronic detector based on MoS_2/InAlAs/InGaAs n-i-n heterojunction for both visible and near-infrared bands. The detector works under negative bias with the responsivity of 6×10^5 A W^{-1} in visible light and 8×10^5 A W^{-1} in near-infrared illumination of 1550 nm, respectively. Such high responsivities are achieved thanks to the photogating effect and internal amplification of the device, which are carefully discussed by the band bending model. Under positive gate voltage biases, however, abnormal photoelectron responsivity to visible illumination appears. The so-called negative responsivity of -4×10^5 A W^{-1} at $V_g = +1$ V is observed, which is ascribed by the combination of the photoconductance effect in the vertical MoS_2/InAlAs/InGaAs n-i-n heterojunction with the photogating effect in the lateral phototransistor. Such an architecture of the device by integrating two different materials in one substrate opens up a new avenue toward dual band detection in both visible and NIR wavelengths, which will certainly attract broad attentions from the remote sensing area for the innovation of new generation photoelectronic detectors.

Experimental Section

The device fabrication starts from the mesa isolation of the device by wet etching down to the $In_{0.52}Al_{0.48}As$ buffer layer in a mixture of phosphoric acid (H_3PO_4) and hydrogen peroxide (H_2O_2). Then source/drain electrodes were patterned by electron beam lithography (EBL), and 20 Ti and 200 nm Au were deposited by electron beam evaporation (EBE) to form good Ohmic contact with the heavily n-doped InGaAs capping layer. After that, the bare region between the source/drain electrodes was etched down to the $In_{0.52}Al_{0.48}As$ barrier layer by a two-step etching method. In the first step, the top 20 nm InGaAs capping layer was etched in a mixture of citric acid ($C_6H_8O_7$) and hydrogen peroxide (H_2O_2), and the etching reaction may stop at the InP stopper layer. In the second step, the InP etch stopper was removed in the diluted hydrochloric acid (HCL) solution, and the etching reaction may finally stop at the $In_{0.52}Al_{0.48}As$ barrier layer.

Supporting Information

Supporting Information is available from the Wiley Online Library or from the author.

Acknowledgements

J.D. and L.Z. contributed equally to this work. This work was partially supported by the National Natural Science Foundation of China (Grant Nos. 61574043, No. 11634005 and U1732104), the Basic Research Project of Shanghai Science and Technology Innovation Action (Grant No. 17JC1400300), the Fudan University CIOMP Joint Fund (project number: FC2017-008), and National Key Research and Development Program (2016YFA0203900).

Conflict of Interest

The authors declare no conflict of interest.

Keywords

2D electron gas, dual-band photodetection, gate-tunable negative/positive responsivity, MoS_2/InAlAs/InGaAs van der Waals heterojunction

Received: June 21, 2019
Revised: August 23, 2019
Published online: September 10, 2019

© 2019 WILEY-VCH Verlag GmbH & Co. KGaA, Weinheim

[1] C. Lee, C. Won, M. Bae, J. Shin, J. Lee, S. Hahm, *IEEE Sens. J.* **2015**, *15*, 5071.
[2] J. Seol, S. Kang, C. Lee, C. Won, H. Park, J. Lee, S. Hahm, *IEEE Sens. J.* **2016**, *16*, 6903.
[3] J. Deng, Z. Guo, Y. Zhang, X. Cao, S. Zhang, Y. Sheng, H. Xu, W. Bao, J. Wan, *IEEE Electron Device Lett.* **2019**, *40*, 423.
[4] J. Deng, J. Shao, B. Lu, Y. Chen, A. Zaslavsky, S. Cristoloveanu, M. Bawedin, J. Wan, *IEEE J. Electron Devices Soc.* **2018**, *6*, 557.
[5] C. Huang, C. Ho, M. Wu, *IEEE Electron Device Lett.* **2015**, *36*, 820.
[6] D. Sun, T. Li, B. Yang, X. Shao, X. Li, Y. Chen, *Opt. Express* **2019**, *27*, 9447.
[7] Y. Zhang, A. Haddadi, A. Dehzangi, R. Chevallier, M. Razeghi, *IEEE J. Quantum Electron.* **2019**, *55*, 1.
[8] P. R. A. Binetti, X. J. M. Leijtens, T. d. Vries, Y. S. Oei, L. D. Cioccio, J. Fedeli, C. Lagahe, J. V. Campenhout, D. V. Thourhout, P. J. v. Veldhoven, R. Nötzel, M. K. Smit, *IEEE Photonics J.* **2010**, *2*, 299.
[9] A. Joshi, S. Datta, *Proc. SPIE* **2012**, *4*, 8385.
[10] Y. Gao, Z. Zhong, S. Feng, Y. Geng, H. Liang, A. W. Poon, K. M. Lau, *IEEE Photonics Technol. Lett.* **2012**, *24*, 237.
[11] P. K. Venuthurumilli, P. D. Ye, X. Xu, *ACS Nano* **2018**, *12*, 4861.
[12] H. Huang, F. Wang, Y. Liu, S. Wang, L.-M. Peng, *ACS Appl. Mater. Interfaces* **2017**, *9*, 12743.
[13] W. Withayachumnankul, C. M. Shah, C. Fumeaux, B. S. Y. Ung, W. J. Padilla, M. Bhaskaran, D. Abbott, S. Sriram, *ACS Photonics* **2014**, *1*, 625.
[14] B. Deng, Q. Guo, C. Li, H. Wang, X. Ling, D. B. Farmer, S. J. Han, J. Kong, F. Xia, *ACS Nano* **2016**, *10*, 11172.
[15] B. Lee, J. Park, G. H. Han, H.-S. Ee, C. H. Naylor, W. Liu, A. T. C. Johnson, R. Agarwal, *Nano Lett.* **2015**, *15*, 3646.
[16] M. Chhowalla, D. Jena, H. Zhang, *Nat. Rev. Mater.* **2016**, *1*, 16052.
[17] H. S. Lee, S.-W. Min, Y.-G. Chang, M. K. Park, T. Nam, H. Kim, J. H. Kim, S. Ryu, S. Im, *Nano Lett.* **2012**, *12*, 3695.
[18] D. Lembke, S. Bertolazzi, A. Kis, *Acc. Chem. Res.* **2015**, *48*, 100.
[19] K. S. Novoselov, A. Mishchenko, A. Carvalho, A. H. Castro Neto, *Science* **2016**, *353*, aac9439.
[20] S. Jang, E. Hwang, Y. Lee, S. Lee, J. H. Cho, *Nano Lett.* **2015**, *15*, 2542.
[21] Y. Shao, Y. Liu, X. Chen, C. Chen, I. Sarpkaya, Z. Chen, Y. Fang, J. Kong, K. Watanabe, T. Taniguchi, A. Taylor, J. Huang, F. Xia, *Nano Lett.* **2017**, *17*, 7330.
[22] Y. Lee, J. Kwon, E. Hwang, C.-H. Ra, W. J. Yoo, J.-H. Ahn, J. H. Park, J. H. Cho, *Adv. Mater.* **2015**, *27*, 41.
[23] Y. Han, X. Zheng, M. Fu, D. Pan, X. Li, Y. Guo, J. Zhao, Q. Chen, *Phys. Chem. Chem. Phys.* **2016**, *18*, 818.
[24] H. H. Fang, W. D. Hu, *Adv. Sci.* **2017**, *4*, 1700323.
[25] D. Yun, H. Jo, S. Son, J. Baek, J. Lee, T. Kim, D. Kim, T. Tsutsumi, H. Sugiyama, H. Matsuzaki, *IEEE Electron Device Lett.* **2018**, *39*, 1844.
[26] T. Takahashi, Y. Kawano, K. Makiyama, S. Shiba, M. Sato, Y. Nakasha, N. Hara, *IEEE Trans. Electron Devices* **2017**, *64*, 89.
[27] P. Ding, C. Chen, M. Asif, X. Wang, J. Niu, F. Yang, W. Ding, Y. Su, D. Wang, Z. Jin, *IEEE J. Electron Devices Soc.* **2018**, *6*, 49.
[28] C. Chang, H. Hsu, E. Y. Chang, C. Kuo, S. Datta, M. Radosavljevic, Y. Miyamoto, G. Huang, *IEEE Electron Device Lett.* **2007**, *28*, 856.
[29] Y. Takanashi, K. Takahata, Y. Muramoto, *IEEE Trans. Electron Devices* **1999**, *46*, 2271.
[30] C. Lee, B. Chou, W. Hsu, *IEEE Trans. Electron Devices* **2011**, *58*, 725.
[31] C. Choi, H. Kang, C. Woo-Young, H. Kim, W. Choi, D. Kim, K. Jang, K. Seo, *IEEE Photonics Technol. Lett.* **2003**, *15*, 846.
[32] C. Lin, H. Chiu, C. Lin, H. Wang, Y. Wu, *J. Lightwave Technol.* **2010**, *28*, 2153.
[33] C. Chang-Soon, K. Hyo-Soon, C. Woo-Young, K. Dae-Hyun, S. Kwang-Seok, *IEEE Trans. Microwave Theory Tech.* **2005**, *53*, 256.
[34] A. K. Okyay, D. Kuzum, S. Latif, D. A. B. Miller, K. C. Saraswat, *IEEE Trans. Electron Devices* **2007**, *54*, 3252.
[35] S. H. Yu, Y. Lee, S. K. Jang, J. Kang, J. Jeon, C. Lee, J. Y. Lee, H. Kim, E. Hwang, S. Lee, J. H. Cho, *ACS Nano* **2014**, *8*, 8285.
[36] R. Saran, R. J. Curry, *Nat. Photonics* **2016**, *10*, 81.

© 2019 WILEY-VCH Verlag GmbH & Co. KGaA, Weinheim